

1        **Technical Note: Monitoring discharge of mountain streams by**  
2                    **retrieving image features with deep learning**

3    Chenqi Fang<sup>1</sup>, Genyu Yuan<sup>1</sup>, Ziyang Zheng<sup>1</sup>, Qirui Zhong<sup>1</sup>, Kai Duan<sup>1\*</sup>

4    <sup>1</sup> *School of Civil Engineering, Sun Yat-Sen University, Guangzhou, China*

5    \*Corresponding author, E-mail: duank6@mail.sysu.edu.cn

## 6 **Abstract**

7 Traditional discharge monitoring usually relies on measuring flow velocity and cross-  
8 section area with various velocimeters or remote-sensing approaches. However, the  
9 topography of mountain streams in remote sites largely hinders the applicability of  
10 velocity-area methods. We here present a method to continuously monitor mountain  
11 stream discharge using a low-cost commercial camera and deep learning algorithm. A  
12 procedure of automated image categorization and discharge classification was  
13 developed to extract information on flow patterns and volumes from high-frequency  
14 red–green–blue (RGB) images with deep convolutional neural networks (CNNs). The  
15 method was tested at a small, steep, natural stream reach in southern China. Reference  
16 discharge data was acquired from a V-shaped weir and ultrasonic flowmeter installed a  
17 few meters downstream of the camera system. Results show that the discharge-relevant  
18 stream features implicitly embedded in RGB information can be effectively recognized  
19 and retrieved by CNN to achieve satisfactory performance in discharge measurement.  
20 Coupling CNN and traditional machine learning models (e.g., support vector machine  
21 and random forest) can potentially synthesize individual models’ diverse merits and  
22 improve generalization performance. Besides, proper image pre-processing and  
23 categorization are critical for enhancing the robustness and applicability of the method  
24 under environmental disturbances (e.g., weather and vegetation on river banks). Our  
25 study highlights the usefulness of deep learning in analyzing complex flow images and  
26 tracking flow changes over time, which provides a reliable and flexible alternative



27 apparatus for continuous discharge monitoring of rocky mountain streams.

28 **Keywords:**

29 Discharge monitoring; Mountain streams; Deep learning; Machine learning; Image  
30 categorization

## 31 **1 Introduction**

32 Continuous discharge data is critical for hydrological model development and flood  
33 forecast (Clarke, 1999; Mcmillan et al., 2010), water resources management (Council,  
34 2004), and aquatic ecosystem health assessment (Carlisle et al., 2017). Traditional  
35 discharge monitoring relies on stream gauges that convert water level to discharge with  
36 an established stage-discharge curve, or information on stable cross-sections and flow  
37 velocity obtained from flow velocimeters such as Acoustic Doppler Current Profiler  
38 (ADCP) and ultrasonic defectoscope (Kasuga et al., 2003). However, these approaches  
39 require significant investment on the implementation of equipments, training of  
40 personnel with expertise, and constant maintenance (Fujita et al., 2007; Czuba et al.,  
41 2017; Yorke and Oberg, 2002). Besides, the performance of transducers and  
42 velocimeters is usually susceptible to sediments and floating debris, particularly in  
43 flooding seasons (Hannah et al., 2011). Consequently, large temporal gaps remain in  
44 many discharge records across the world despite of the growing demand on data  
45 (Davids et al., 2019; Royem et al., 2012). Spatially, flow monitoring of downstream  
46 river sections has been assigned to a higher priority due to the concerns on water supply  
47 and flood control, leading to an acute shortage of discharge data in mountain streams

48 and headwater catchments (Deweber et al., 2014).

49 To overcome the limitations of traditional methods, a few image-based approaches  
50 have been introduced into water stage, flow velocity, and discharge measurement in  
51 rivers (Noto et al., 2022; Leduc et al., 2018). Image-based (Leduc et al., 2018; Noto et  
52 al., 2022) approaches rely only on the acquisition of digital images of streams from  
53 inexpensive commercial cameras and thus have been a promising alternative for  
54 continuous, noninvasive, and low-cost streamflow monitoring. The two most  
55 commonly used approaches include large-scale particle image velocimetry (LSPIV)  
56 and particle tracking velocimetry (PTV). LSPIV (Fujita et al., 2010) is based on a high-  
57 speed cross-correlation scheme between an interrogation area (IA) in a first image and  
58 IAs within a search region (SR) in a second image. The technique has been proved  
59 effective in monitoring low-velocity and shallow-depth flow fields (Tauro et al., 2018).  
60 However, it performs poorly in mapping velocity fields in high resolution when there  
61 is a lack of seeds on the water surface because the algorithm obtains the average speed  
62 of each SR (Tauro et al., 2017). Compared to LSPIV, PTV was designed for low seeding  
63 density flows, focusing on particle tracking instead of recognition. The PTV approach  
64 does not require assumptions on flow steadiness nor the relative position of neighbor  
65 particles (Tauro et al., 2018). Several algorithms have been developed for PTV analysis,  
66 such as space-time image velocimetry (STIV) and optical tracking velocimetry (OTV),  
67 overcoming the over-dependence on natural particles' shape and size (Tauro et al., 2018;  
68 Tsubaki, 2017). STIV evaluates surface flow velocity by analyzing a texture angle

69 within a variation of brightness or color on the water surface, while OTV combines  
70 automatic feature detection, Lucas-Kanade tracking algorithm and track-based filtering  
71 methods to estimate subpixel displacements (Fujita et al., 2007; Karvonen, 2016).  
72 Existing image-based discharge measurement methods all use the velocity-area method  
73 to indirectly deduce discharge after identifying stage and average (Davids et al., 2019;  
74 Leduc et al., 2018; Tsubaki, 2017; Herzog et al., 2022) velocity. The average velocity  
75 in a cross-section is estimated with surface velocity derived from natural or artificial  
76 seeds on water surface and pre-defined empirical relationships between the surface  
77 velocity and average velocity. The velocity-area method relies on a stable relationship  
78 between stage and cross-sectional area, and needs to take velocity extrapolations to the  
79 edges and vertical distributions throughout the cross-section into account (Le Coz et al.,  
80 2012). However, it is difficult to identify the water stage and vertical characteristics of  
81 mountain streams due to the steep, narrow, and highly heterogeneous cross-sections.  
82 The applicability of PIV and PTV approaches is largely hindered by such topography.

83 Unlike PIV and PTV, deep learning models possess the capability to extract  
84 discharge-related features from images of rivers or streams automatically. These models  
85 are able to adjust the weights assigned to each feature, eliminating the need for manual  
86 attention and reducing the risk of overemphasizing or misinterpreting features that are  
87 unresponsive to flow discharge (Canziani et al., 2016). Besides, deep learning models  
88 can extract low-level image features, such as edges, textures, and colors (Jiang et al.,  
89 2021). These merits could be essential in retrieving information from images of

90 mountain streams, particularly in regions with intricate cross-sectional profiles. For  
91 example, Ansari et al. (2023) developed a convolutional neural network (CNN) to  
92 estimate the spatial surface velocity distribution and derive discharge, outperforming  
93 traditional optical flow methods both in laboratory and field settings, albeit with a  
94 reliance on surveyed cross-section information.

95 In this study, we propose a novel mountain stream discharge monitoring method  
96 using a low-cost commercial camera and deep learning models. Automated image  
97 categorization and pre-processing procedures were developed for processing high-  
98 frequency red–green–blue (RGB) images, and then CNN was used to extract  
99 information on flow patterns from RGB matrices and establish empirical relationships  
100 with the classification probabilities of discharge volumes. We hypothesize that (1) the  
101 features of mountain streams (e.g., coverage of water surface, flow direction, flow  
102 velocity) embedded in RGB images can be recognized by suitable deep learning  
103 approaches to achieve effective discharge monitoring, and (2) proper image pre-  
104 processing and categorization can improve accuracy of image-based discharge  
105 monitoring of mountain streams. A rocky mountain stream of a headwater catchment in  
106 tropical southern China was used as a study site to test our hypotheses.

107

## 108 **2 Methods**

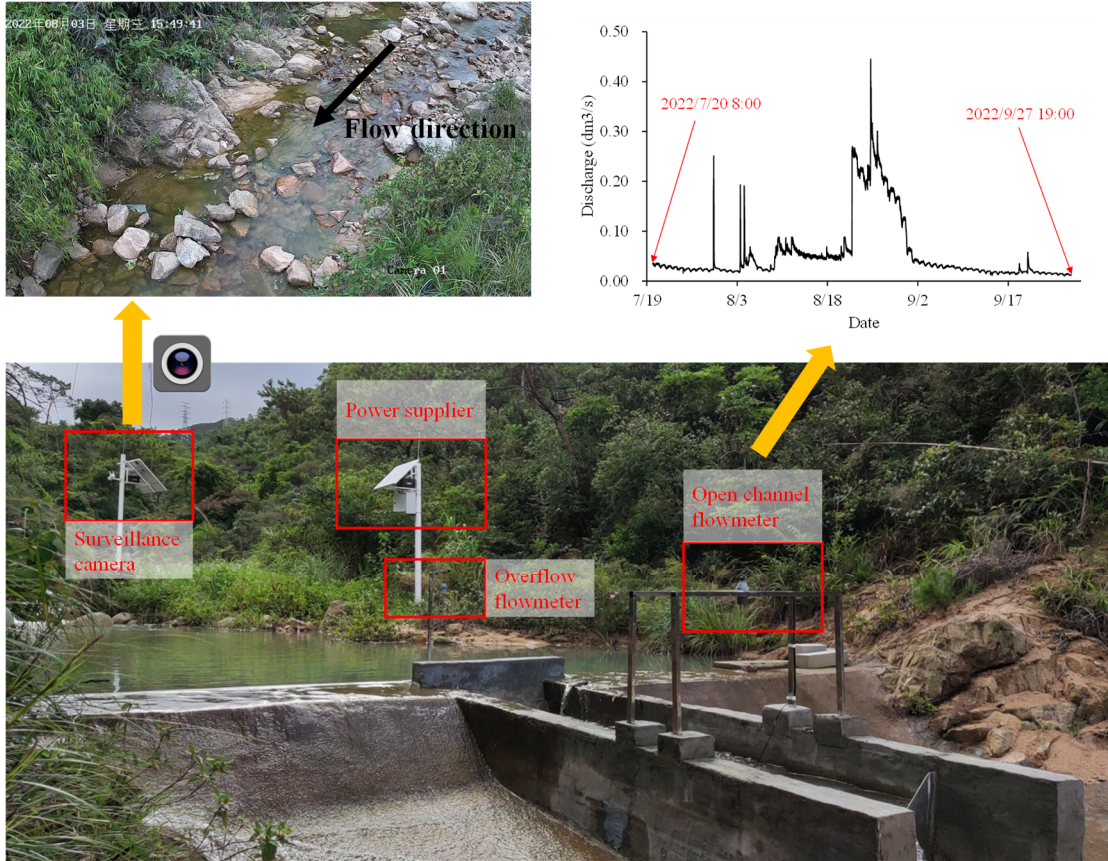
### 109 **2.1 Site and field setting**

110 The study site is located on a small, steep, rocky reach of a stream in the Zhuhai Campus

111 of Sun Yat-sen University, China (22°20'58" N, 113°34'29" E). The site elevation is 13  
112 m above sea level and about 2 km away from the Lingding Yang of South China Sea.  
113 The stream flow is mainly controlled by rainfall in the upstream drainage area. Water  
114 stage and flow velocity increase rapidly during East Asian summer monsoon rainfalls  
115 and fluctuate with synoptic weather conditions on dry days.

116 The main objective of the study was to test the applicability of deep-learning based  
117 image processing approaches in capturing the flow characteristics and discharge  
118 volumes in the daily flow cycle in this mountain stream. We selected a straight, single-  
119 thread reach for the gauging location, and set up a Hikvision camera on the left bank of  
120 the stream to collect flow images (**Fig. 1**). Discharge data monitored by a weir about 8  
121 m downstream of the camera was used for model training and validation. The camera  
122 was installed 3 m above the ground, facing the surface of the stream almost vertically.  
123 The entire stream width is visible in the images. The camera was equipped with a 150W  
124 solar panel and 80AH lithium battery, enabling the camera to work continuously for 80  
125 hours without external power on rainy days. The camera supports the wireless  
126 transmission of video data to the server.

127



128

129 **Figure 1.** Camera setup. The camera is set on the left bank of the stream, about 3 m

130 above the water surface, and 8 m upstream of a gauging weir. The top right panel

131 demonstrates the changes in the flowmeter’s discharge during the measurement period.

132

### 133 2.2 Data

134 The flat V-shaped weir downstream of the camera monitors discharge with an open

135 channel flowmeter and an overflow flowmeter. The flowmeters measure water levels in

136 the channel and in front of the weir with ultrasonic sensors and calculate real-time

137 discharge at the time step of two minutes by a semi-empirical equation suggested by

138 the State Bureau of Technical Supervision of China ([www.chinesestandard.net](http://www.chinesestandard.net)), as

139 
$$Q = \frac{8}{15} C_e \tan \frac{\theta}{2} \sqrt{2gh_e^{\frac{5}{2}}} \quad (1)$$

140 where  $Q$  is the discharge of stream,  $\theta$  is the angle of triangular weir,  $g$  is  
141 acceleration of gravity,  $h_e$  is the height of the water surface from the bottom of triangle  
142 barrier,  $C_e$  is an empirical coefficient.

143 We collected the discharge data of the weir (**Fig. 1**) and its corresponding stream  
144 videos during daylight (07:00-19:00 UTC+8) from July 20<sup>th</sup> to September 27<sup>th</sup>, 2022.  
145 The raw video resolution was 2560×1440 pixels with a refresh rate of 50 Hz. Images  
146 were extracted from the videos at 5-minute intervals to avoid excessive similarity  
147 between adjacent images. A total of 7,757 image samples labeled with 37 discharge  
148 values between 0.014 and 0.050 m<sup>3</sup>/s at the interval of 0.001 m<sup>3</sup>/s were collected for  
149 model testing.

## 150 **2.3 Image processing**

### 151 **2.3.1 Image categorization**

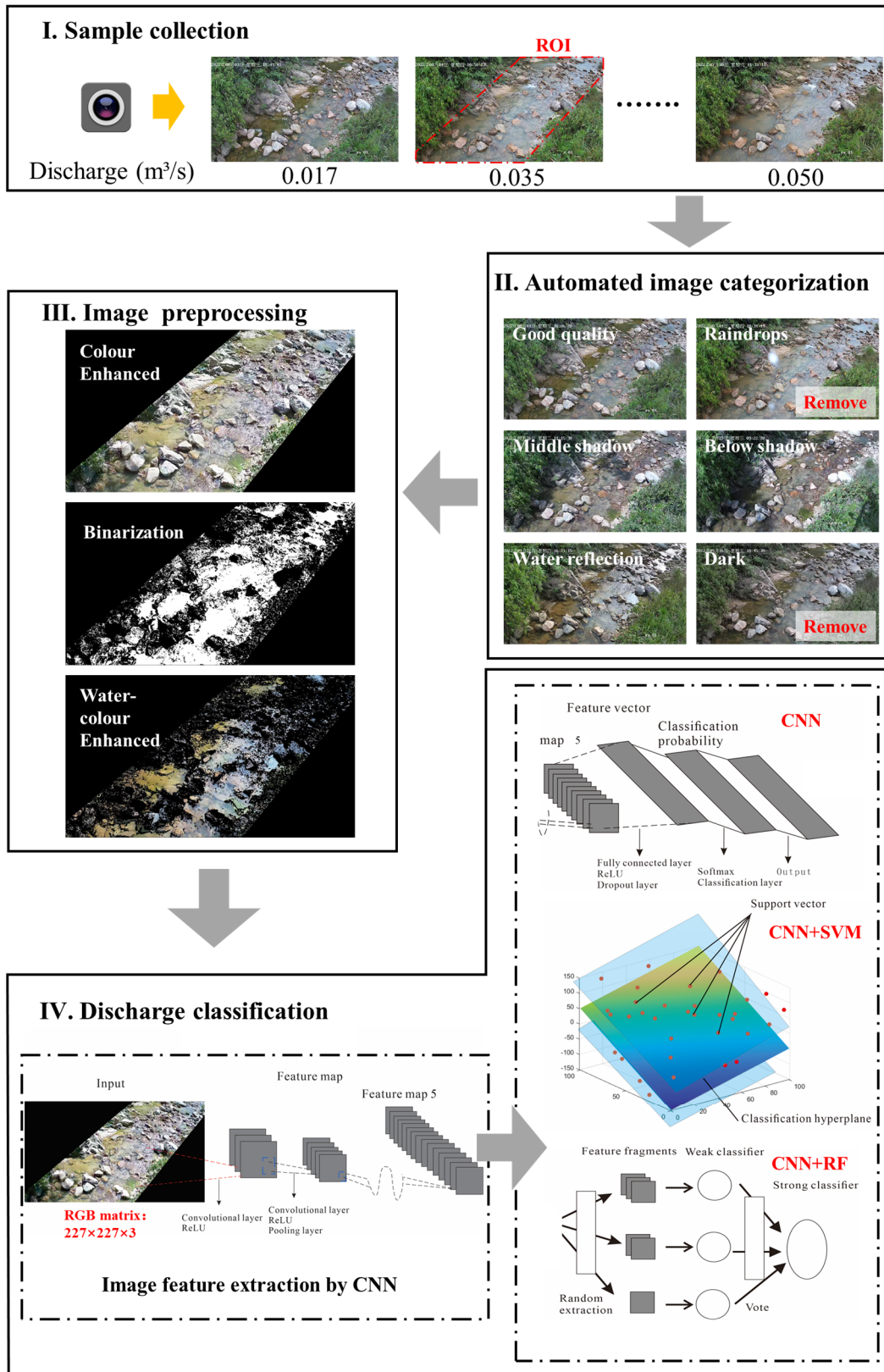
152 Environmental disturbances such as illumination and shadow can seriously interfere  
153 with the extraction of effective image features of mountain streams, such as boundaries  
154 of water surface and textures of flow lines (Herzog et al., 2022; Gershon et al., 1986).  
155 Although researchers have proposed methods to eliminate shadows (Finlayson et al.,  
156 2002), the treatment effect in some complex environments, such as plant shadows and  
157 boulders distributed on mountain streams, is not always satisfactory.

158 Frequently observed disturbances on images include: (1) shadows in the target stream  
159 region due to plants blocking direct sunlight; (2) image noise due to raindrops attached

160 to the camera lens on rainy days; (3) the lack of light leading to low brightness and  
161 contrast of the image; (4) overexposure of image due to light reflection of the water  
162 surface (around 16:00 UTC+8 in this case). Taking these factors into consideration, we  
163 divided all image samples into six categories, including "Good quality", "Raindrops",  
164 "Middle shadow", "Below shadow", "Water reflection", and "Dark" (**Fig. 2**). "Good  
165 quality" contains image samples without obvious noise or shadow. All the other images  
166 lose some feature information due to noise, shadows, reflections, or dim lighting. To  
167 ensure the model performance under different environmental conditions, we designed  
168 an automated categorization procedure (**Fig. 3**) to screen the raw images and exclude  
169 the "Raindrops" and "Dark" samples from model training.

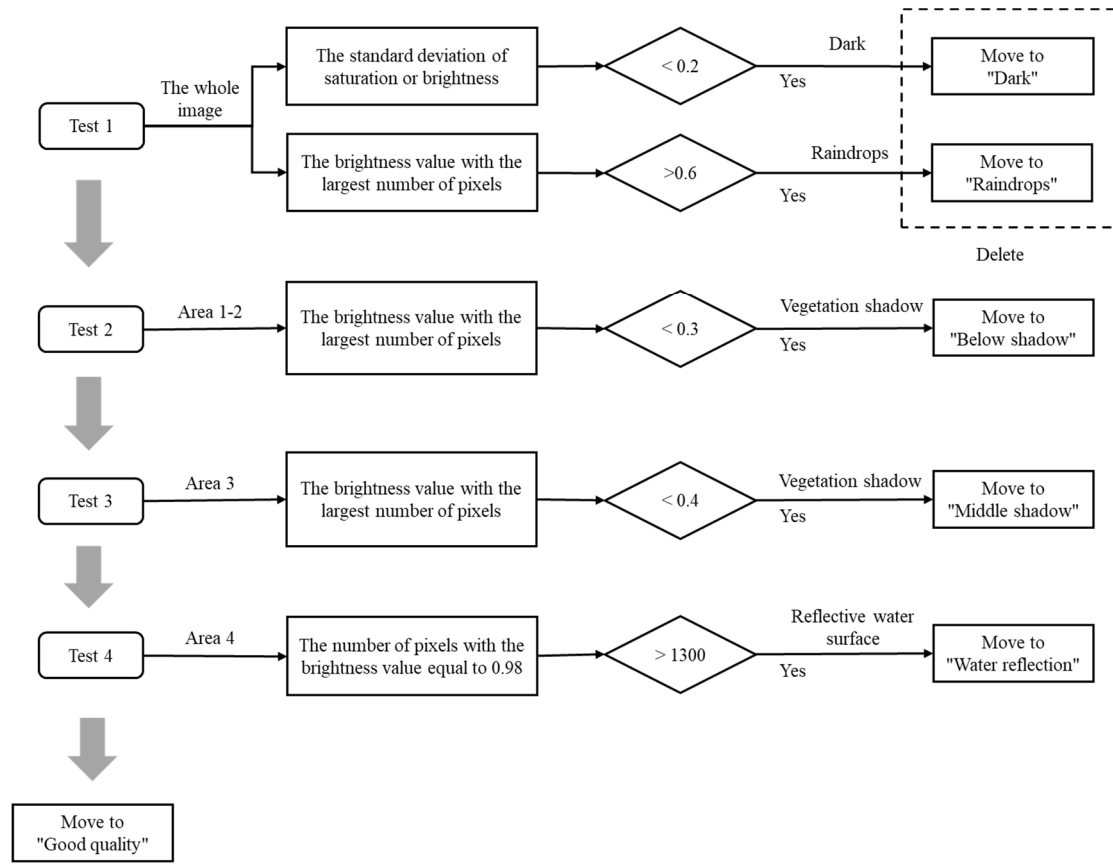
170





171

172 **Figure 2.** Flowchart of image processing and discharge monitoring.



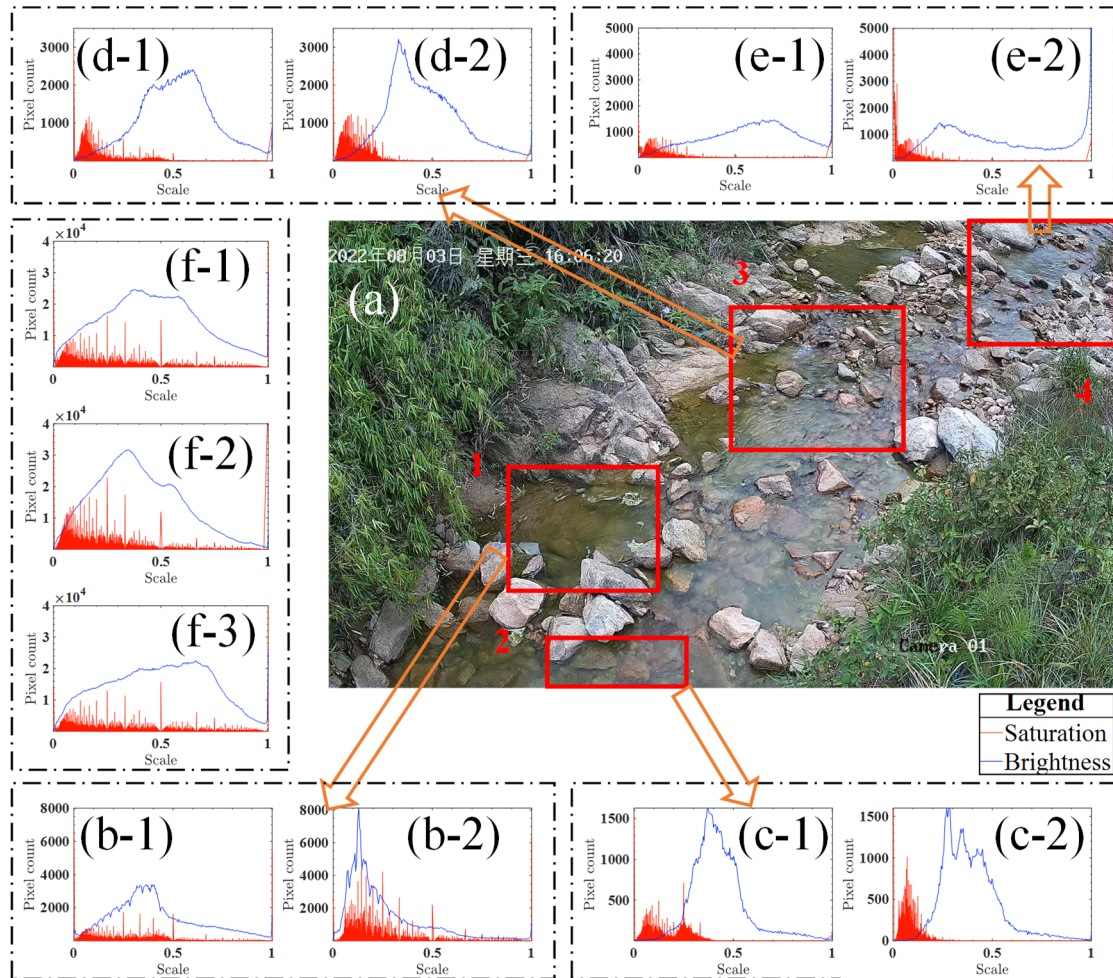
174

175 **Figure 3.** Procedure of automated image categorization.

176

177 Firstly, we selected four areas in the image as the detection areas (**Fig. 4a**) where the  
 178 special conditions mentioned above commonly occurred: the upper and lower shadows  
 179 in the target stream section mainly appeared in Area 3 and Area 1&2, respectively;  
 180 disturbance of water surface reflection was mostly found in Area 4. Then, the thresholds  
 181 of saturation or brightness in the four detection areas for image categorization were  
 182 determined manually by comparing image samples under different conditions. The  
 183 four-step procedure includes: (1) "Dark" images (**Fig. 4f-2**) were identified when the  
 184 standard deviation of the brightness or saturation of the full image was less than 0.2. (2)

185 "Raindrops" images (**Fig. 4f-3**) were identified when the brightness of the whole image  
186 with the largest number of pixels was greater than 0.6. These two types of images were  
187 excluded from the training samples. (3) "Below shadow" (**Fig. 4b-2; Fig. 4c-2**) and  
188 "Middle shadow" images (**Fig. 4d-2**) were identified when the brightness value with  
189 the largest number of pixels in Area 1&2 and Area 3 was less than 0.3 and 0.4,  
190 respectively. (4) "Water reflection" images were identified when the number of pixels  
191 with a brightness value of 0.98 in Area 4 exceeded 1300 (**Fig. 4e-2**). The images passing  
192 all the tests in the procedure were considered "Good quality" samples. The other charts  
193 in **Fig. 4** show the saturation and brightness distributions derived from a typical "Good  
194 quality" image.



195

196 **Figure 4.** Comparison of saturation and brightness distributions in the four detection  
 197 areas under different environmental conditions. The horizontal axis is the interval range  
 198 (0-1) of saturation and brightness in HSB space. The vertical axis indicates the number  
 199 of pixels under a certain saturation or brightness value. Figures b-1, c-1, d-1, and e-1  
 200 display the saturation and brightness distributions in Area 1-4 of a “Good quality”  
 201 sample. Figures b-2, c-2, d-2, and e-2 display the results derived from samples of  
 202 “Below shadow” (b-2; c-2), “Middle shadow” (d-2), and “Water reflection” (e-2),  
 203 respectively. Figures f-1, f-2, and f-3 display the saturation and brightness distributions  
 204 of an entire image, derived from “Good quality”, “Dark”, and “Raindrops” samples,

205 respectively.

206

### 207 **2.3.2 Color enhancement**

208 In order to highlight the stream features embedded in the images and avoid image  
209 information redundancy, we compared three commonly used color enhancement  
210 approaches to process the image samples.

211 **(1) Color Enhanced.** A dynamic histogram equalization technique (Abdullah-Al-  
212 Wadud et al., 2007; Cheng and Shi, 2004) was used to enhance contrast and emphasize  
213 stream features. First, vegetation areas on both sides of the stream were cropped and  
214 filled with black. Then, histogram equalization was used to enhance the contrast  
215 between light and dark, i.e., brighten the bubbles, swirls, ripples, splashes, water  
216 coverage, etc., and darken the bottom stones and reflections in the water.

217 **(2) Binarization.** Binarization of image information can decrease the  
218 computational load and enable the utilization of simplified methods compared to 256  
219 levels of grey-scale or RGB color information (Finlayson et al., 2002; Sauvola and  
220 Pietikäinen, 2000). In this case, the RGB and HSB (Hue, Saturation, Brightness)  
221 information extracted from images suggests that the brightness of the stream water  
222 under daylight ranges from 0.2 to 0.7, and the values of three color components follow:

$$223 \quad R(x, y) + G(x, y) + B(x, y) > 350 \quad (2)$$

224 Where  $R(x, y)$ ,  $G(x, y)$  and  $B(x, y)$  respectively represent the red, green, and blue  
225 color values of the pixel  $(x, y)$ . The original image was transformed into a binary image

226 by assigning the values of "1" and "0" to the pixels within and out of the water body,  
227 respectively.

228 **(3) Water-color Enhanced.** Considering that water-color features may carry some  
229 useful information on discharge (Kim et al., 2019), we tested a new pre-processing  
230 method combining the two approaches above. The RGB information of the original  
231 image within the water body areas was kept unchanged, while the non-water body areas  
232 were filled with black color. Then, the water body areas were further enhanced with the  
233 histogram equalization method to highlight the edge transition between the water body  
234 and the background (Abdullah-Al-Wadud et al., 2007).

### 235 **2.3.3 Image denoising**

236 Images pre-processed by all of three approaches still contain large amounts of noise  
237 due to environmental disturbances and edge oversharpening caused by image contrast  
238 enhancement (Herzog et al., 2022). Therefore, the wavelet transform (Zhang, 2019) was  
239 adopted to denoise the image samples. We chose a compromise threshold between hard  
240 and soft thresholds as the threshold function (Chang et al., 2010). When the wavelet  
241 coefficient is greater than or equal to the threshold, a compromise coefficient  $\alpha$  ranging  
242 from 0 to 1 is added before the threshold to achieve a smooth transition from hard to  
243 soft thresholds, as

$$244 \quad \lambda = \frac{\text{median}(d_j(k))}{0.6745} \times \sqrt{2 \log(M \times N)} \quad (3)$$

$$245 \quad \omega_\lambda = \begin{cases} [\text{sign}(\omega)](|\omega| - \alpha\lambda), & |\omega| \geq \lambda \\ 0, & |\omega| < \lambda \end{cases} \quad (4)$$

246 where  $j$  is the scale of wavelet decomposition,  $d_j(k)$  is the coefficient of wavelet

247 decomposition,  $M$  and  $N$  are the length and width of images,  $\omega$  is the wavelet  
248 coefficient,  $\lambda$  is the set threshold, and  $sign$  is the sign function. In this case,  $M \times$   
249  $N=2560 \times 1440$ ,  $\alpha=0.5$ .

## 250 **2.4 Correlation between color information and discharge**

251 The unstructured image data of mountain streams implicitly contains many stream  
252 features relevant to discharge, such as the width and depth of streams, the coverage of  
253 water surface, and spatial distributions of flow direction and flow velocity. In this study,  
254 we attempted to achieve discharge monitoring by establishing empirical relationships  
255 between the RGB color information of the water body and the discharge volumes. We  
256 first explored the correlation between the combination of R/G/B values ( $a\bar{R} + b\bar{G} +$   
257  $c\bar{B}$ , where  $\bar{R}$ ,  $\bar{G}$ ,  $\bar{B}$  are the mean values of red, green and blue channels of an image,  
258 respectively, and  $a$ ,  $b$ , and  $c$  are coefficients to be determined) in the region of interest  
259 (ROI, see **Fig. 2**) and the discharge conditions. Spearman's rank correlation coefficient  
260 between  $a\bar{R} + b\bar{G} + c\bar{B}$  and discharge is calculated as

$$261 \quad r_s = 1 - \frac{6 \sum_{i=1}^n d_i^2}{n(n^2-1)} \quad (5)$$

262 where  $n$  is the number of samples,  $d_i$  is the difference between the ranks of R/G/B values  
263 and discharge of each image sample.

264

## 265 **2.5 Algorithms of discharge estimation**

266 We used three algorithms to establish discharge classification models (**Fig. 2**), including  
267 convolutional neural network (CNN), support vector machine (SVM), and random

268 forest (RF). The data of the RGB color matrix derived from pre-processed images was  
269 used as model inputs. SVM and RF were coupled with CNN to explore the potential  
270 merits of traditional machine learning algorithms in improving the classification  
271 accuracy and efficiency of CNN-based discharge classifiers. All the embedding image  
272 features are normalized and regularized before passed to classifiers to avoid overfitting  
273 for CNN-based models.

### 274 **2.5.1 Convolutional Neural Network (CNN)**

275 Deep convolutional neural network allows computational models composed of multiple  
276 processing layers to learn representations of data with multiple levels of abstraction,  
277 which have brought breakthroughs in processing images, video, speech, and audio  
278 (Lecun et al., 2015). The AlexNet architecture (Krizhevsky et al., 2017) was used to  
279 construct our model. Parameters of the semantic layer of the model were calibrated to  
280 achieve feature extraction and classification of stream images. The image size was first  
281 rescaled from 2560×1440 to 227×227 to facilitate the migration of trained AlexNet. A  
282 227×227×3 (length×width×color) matrix was retrieved from each image as the model  
283 input. There were five built-in convolutional layers, using a 3×3 convolution kernel and  
284 a 3×3 pooled kernel. We replaced the last three layers of AlexNet with a full-connection  
285 layer, a softmax layer, and a classification layer, leaving all other layers intact. The  
286 parameters of the full-connection layer were set according to the number of selected  
287 discharge values. The ReLU function was used as the convolutional layer activation  
288 function to extract and pass on the water coverage features. The SoftMax function was



289 the activation function of the output layer, and the extracted feature vectors were  
 290 compressed under each discharge label. The probability that a stream image falls into a  
 291 discharge label was calculated as

$$292 \quad P(y|x) = \frac{e^{h(x,y_i)}}{\sum_{i=1}^n e^{h(x,y_i)}} \quad (6)$$

293 where  $x$  is the feature vector extracted by CNN,  $y$  is the discharge label,  $n$  is the number  
 294 of labels,  $h(x, y_i)$  is the linear connectivity function. The training method for CNN  
 295 was stochastic gradient descent with momentum, with 15 samples in small batches, a  
 296 maximum number of rounds of 10, a validation frequency of 3 epochs, and an initial  
 297 learning rate of 0.00005. The samples were shuffled in every epoch. The loss function  
 298 for discharge classification was Cross-Entropy Loss, as

$$299 \quad L = -\frac{1}{N} \sum_{i=1}^N \sum_{c=1}^C y_{i,c} \log(p_{i,c}) \quad (7)$$

300 where  $L$  is the value of loss,  $N$  is the number of samples,  $C$  is the number of discharge  
 301 classes,  $y_{i,c}$  represents the value of the true label for the  $i^{\text{th}}$  sample in the  $c^{\text{th}}$  class using  
 302 one-hot encoding, and  $p_{i,c}$  represents the probability of  $i^{\text{th}}$  sample belonging to  $c^{\text{th}}$   
 303 class calculated by CNN.

304

### 305 **2.5.2 Convolutional Neural Network coupled with Support Vector Machine** 306 **(CNN+SVM)**

307 SVM is a machine learning method based on structural risk minimization and Vapnik–  
 308 Chervonenkis (VC) dimension theory (Cortes and Vapnik, 1995). It has been widely  
 309 used in image processing, pattern recognition, fault diagnosis, prediction and

310 classification (Burges, 1998), which can help to capture key samples and eliminate  
311 redundant samples by finding the optimal hyperplane. Compared with neural networks,  
312 which rely on large training samples and tend to fall into local optima, SVM can achieve  
313 global optima with a simpler model structure (Hanczar et al., 2010; Matykiewicz and  
314 Pestian, 2012). However, the SVM-based classifier requires manual input of image  
315 features. Therefore, we coupled CNN and SVM to achieve automatic discharge  
316 classification. Image features extracted by CNN (i.e., the output of the 5<sup>th</sup> CNN pooling  
317 layer) were fed into SVM classifiers to calculate discharge. The extracted image  
318 features, coded with a "one-vs-all" scheme, were used to train binary SVM classifiers.  
319 Specifically, one SVM classifier with a linear kernel function was trained for each  
320 discharge class to distinguish that class from the rest. The hinge loss function was  
321 employed to optimize the entire model by maximizing the margin between discharge  
322 classes.

323

#### 324 **2.4.3 Convolutional Neural Network coupled with Random Forest (CNN+RF)**

325 RF (Tin Kam, 1995) is a flexible machine-learning algorithm that combines the output  
326 of multiple decision trees to reach a single result. Each decision tree depends on the  
327 values of a random vector sampled independently and with the same distribution for all  
328 trees in the forest (Breiman, 2001; Panda et al., 2009). It is an integrated algorithm of  
329 the Bagging type (Aslam et al., 2007) that combines multiple weaker classifiers, and  
330 the final result is obtained by voting or averaging to improve accuracy and

331 generalization performance. We here used an RF comprising 350 decision trees and five  
 332 decision leaves for discharge calculation. The coupling method of CNN+RF mirrors  
 333 that of CNN+SVM, using the same pooling outputs of CNN as inputs for RF discharge  
 334 classifier. RF is trained to assign optimal weights to each decision tree and leaf without  
 335 a specific loss function.

336

## 337 **2.6 Model evaluation metrics**

338 The performance of discharge classification models was measured by four widely used  
 339 metrics, including classification accuracy, F1 score, coefficient of determination ( $R^2$ ),  
 340 and root mean square error (RMSE).

341 (1) Accuracy:

$$342 \quad Accuracy = \frac{\sum_{i=1}^k TP_i}{N} \quad (8)$$

343 where  $TP_i$  is the number of correctly classified samples in the  $i^{\text{th}}$  discharge class;  $N$  is  
 344 the total number of samples;  $k$  is the number of discharge classes.

345 (2) F1 score:

$$346 \quad F1 = \frac{2 \times Precision \times Recall}{Precision + Recall} \quad (9)$$

347 where *Precision* is the ratio of true positive classification ( $TP_i$ ) to the sum of  $TP_i$  and  
 348 the number of misclassified samples with the  $i^{\text{th}}$  discharge simulated by a model ( $FP_i$ );  
 349 *Recall* is the ratio of  $TP_i$  to the sum of  $TP_i$  and the number of misclassified samples  
 350 with the observed  $i^{\text{th}}$  discharge ( $FN_i$ ), calculated as

$$351 \quad Precision = \sum_{i=1}^k \frac{n_i}{N} \times \frac{TP_i}{TP_i + FP_i} \quad (10)$$

352 
$$Recall = \sum_{i=1}^k \frac{n_i}{N} \times \frac{TP_i}{TP_i + FN_i} \quad (11)$$

353 where  $n_i$  is the number of samples that fall in the  $i^{\text{th}}$  class.

354 (3)  $R^2$

355 
$$R^2 = 1 - \frac{\sum_{j=1}^N (y_j - \hat{y}_j)^2}{\sum_{j=1}^N (y_j - Y)^2} \quad (12)$$

356 where  $y_j$  and  $\hat{y}_j$  are the observed and simulated discharge, respectively;  $Y$  is the mean  
357 discharge.

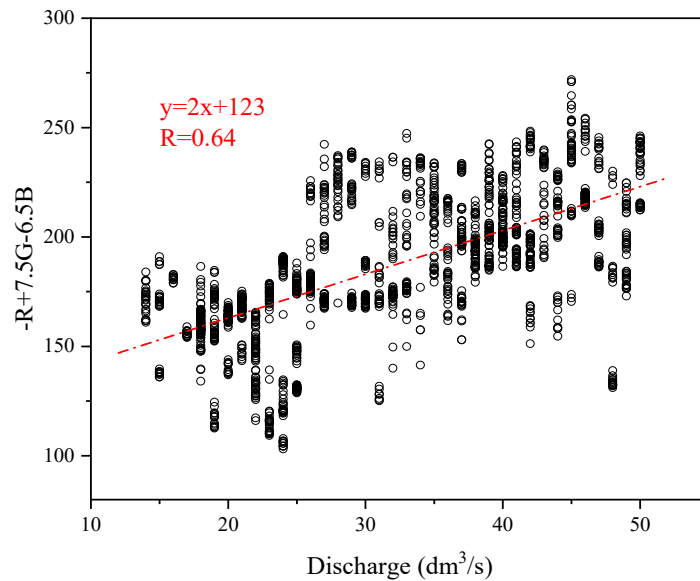
358 (4) RMSE

359 
$$RMSE = \sqrt{\frac{1}{N} \sum_{j=1}^N (y_j - \hat{y}_j)^2} \quad (13)$$

## 360 **3 Results**

### 361 **3.1 Correlation analysis**

362 We first performed a preliminary correlation analysis between the RGB matrices in ROI  
363 and the discharge values. Traversing the common algebraic combinations of the three  
364 colors, we found that  $-\bar{R} + 7.5\bar{G} - 6.5\bar{B}$  ( $\bar{R}$ ,  $\bar{G}$ ,  $\bar{B}$  are the mean values of red, green  
365 and blue channels of an image, respectively) had a spearman correlation coefficient of  
366 0.67 with discharge (p-value < 0.01), indicating that the discharge is significantly  
367 correlated with the color combination value at the 99% confidence level (**Fig. 5**). Such  
368 result suggests that discharge conditions are embedded in RGB information of  
369 mountain streams to some extent, which could be further retrieved and refined by CNN  
370 models.



371

372 **Figure 5.** Correlation between RGB color values and corresponding discharges.

373

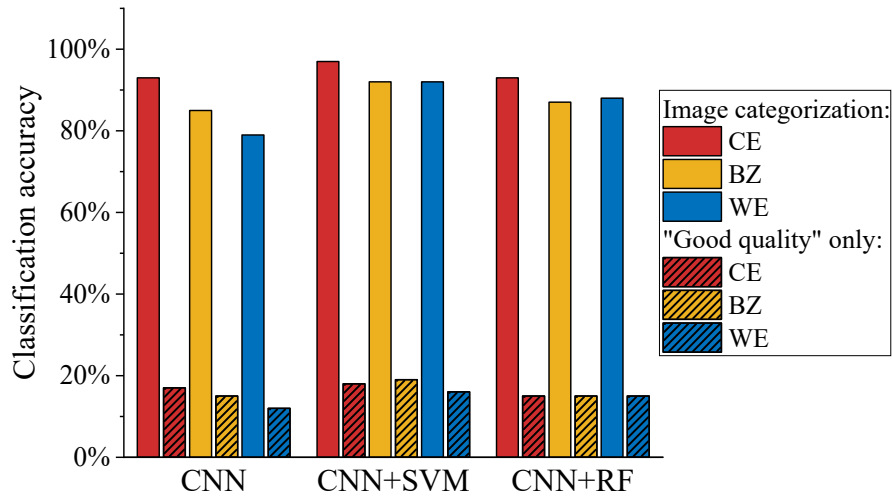
### 374 **3.2 Effectiveness of automated image categorization**

375 Most of the previous image-based studies only selected unblemished images for  
 376 discharge or velocity monitoring, which resulted in poor model performance under  
 377 environmental disturbances (Leduc et al., 2018; Chapman et al., 2020; Herzog et al.,  
 378 2022). In this study, we also included samples under the influence of vegetation  
 379 shadows and water reflection for model training. We selected approximately 100 stream  
 380 images corresponding to each discharge volume (at the interval of 0.001 m<sup>3</sup>/s) from the  
 381 pre-processed samples (3168 images in total). The databases of "Good quality",  
 382 "Middle shadow", "Below shadow", and "Water reflection" were approximately  
 383 sampled in the ratio of 7:0.6:1.4:1 (2146:244:437:341 images) to ensure the  
 384 representation of different environmental conditions. The samples were distributed  
 385 evenly in each discharge interval to avoid bias towards particular discharge conditions

386 and enhance model performance on high and low flows (Wang et al., 2023).

387 **Fig. 6** demonstrates the difference in classification accuracy of monitoring discharge  
388 by the defective images, using two sets of models trained with only "Good quality"  
389 images and samples filtered by automated image categorization, respectively. Results  
390 derived from the three discharge classification models and three color-enhancing  
391 methods consistently suggest that the procedure of automated image categorization can  
392 significantly improve model performance in apprehending defective images.  
393 Classification accuracy of the models trained with only "Good quality" samples  
394 staggered between 11.8%-18.7%, while the accuracy of the models trained after  
395 automated image categorization was higher than 79.0% (79.0%-97.4%) regardless of  
396 the choices of color processing method and deep learning model. The average  
397 difference in classification accuracy between the two sets of training samples reached  
398 73.9%. The proportionate inclusion of defective images with vegetation shadow and  
399 water surface reflection enhances the anti-interference ability of the models in complex  
400 environments.

401



402

403 **Figure 6.** Accuracy of discharge classification of images under environmental  
 404 disturbances. Bars with and without patterns show the results using the models trained  
 405 with only "Good quality" samples and samples after automated image categorization,  
 406 respectively. Color enhancement methods include Color Enhanced (CE), Binarization  
 407 (BZ), and Water-color Enhanced (WE).

408

### 409 3.3 Model training and validation

410 After the treatments of color-enhancing, image denoising, and automated image  
 411 categorization, the images were randomly divided into training and validation sets by  
 412 the ratio of 7:3, and then used for model training and validation, respectively.

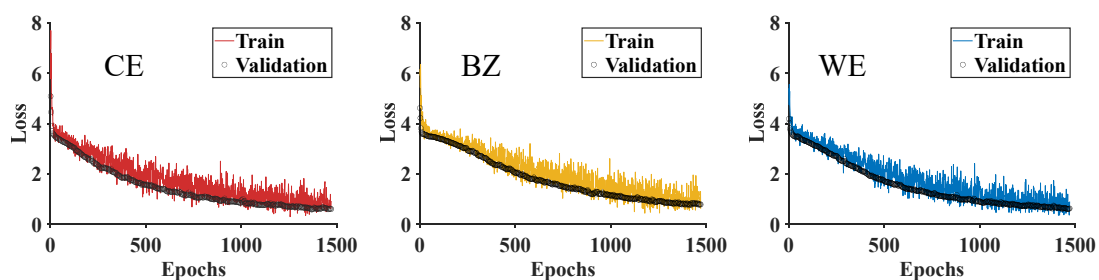
#### 413 3.3.1 Loss changes

414 The changes in training and validation loss of the CNN models driven by three types of  
 415 color-enhanced images are demonstrated in **Fig. 7**. In the initial twenty epochs, the  
 416 training loss values decreased rapidly from 7.70 to 3.73 (Color Enhanced), from 5.91  
 417 to 3.73 (Binarization), and from 5.41 to 3.80 (Water-color Enhanced), respectively.

418 Subsequently, the decreasing rates slowed during the following 1000 epochs, averaging  
419 around -0.0027 to -0.0030 per epoch. The loss value usually stabilizes after 1000 epochs  
420 in CNN training (Keskar et al., 2016). In our case, the loss value began to flatten after  
421 the 1300<sup>th</sup> epoch, signifying convergence towards a consistent loss value below 1.00  
422 across all three color-enhancing methods. Therefore, we set the maximum training  
423 epochs to 1470 to ensure model performance while avoiding overfitting.

424 The proximity between the training and validation loss changes at the final few  
425 epochs is an important indicator that the model is not suffering from overfitting. A  
426 commonly acknowledged benchmark of such proximity is approximately 0.1 to 0.2  
427 (Heaton, 2018). In our CNN models, the validation loss values at the final epoch were  
428 0.60, 0.78, and 0.63, respectively, which were 0.19, 0.08, and 0.07 lower than the  
429 corresponding training loss. Such results suggest that the models did not suffer from  
430 overfitting or underfitting.

431



432

433 **Figure 7.** Changes in training and validation loss of the models driven by three types  
434 of color-enhanced images. Color enhancement methods include Color Enhanced (CE),  
435 Binarization (BZ), and Water-color Enhanced (WE).

436



### 437 3.3.2 Comparison of discharge classification models

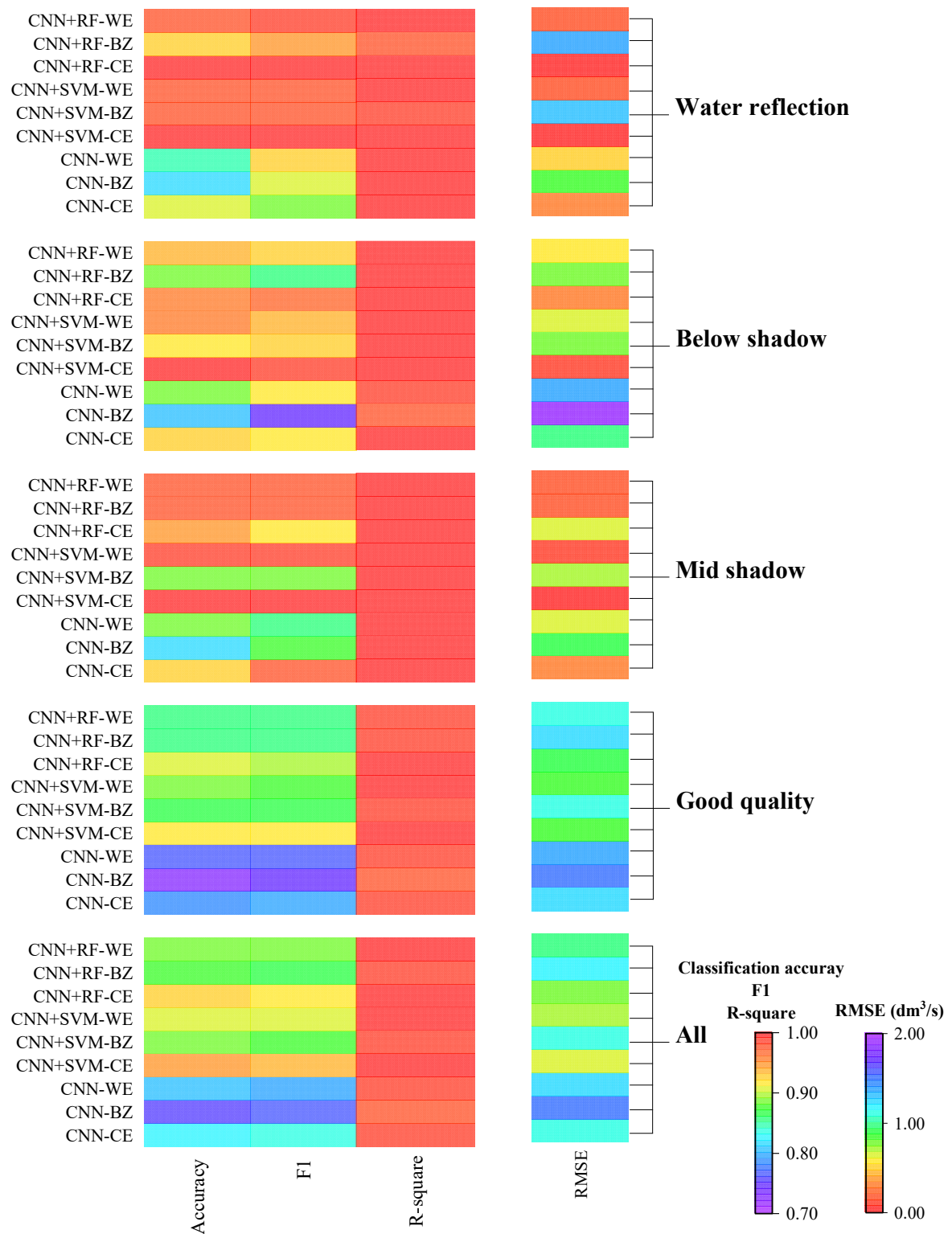
438 The heap map (Fig. 8) visualizes the performance of different models in classifying the  
439 validation image set with three tested color-enhancing methods under different  
440 environmental conditions. Results show that all three models (i.e., CNN, CNN+SVM,  
441 CNN+RF) can achieve satisfactory performance on discharge classification. The  $R^2$   
442 under all environmental conditions was greater than 0.97, suggesting that the simulated  
443 discharge was significantly correlated to the flowmeters' measurement. The comparison  
444 of model performance generally shows consistency under different environmental  
445 conditions. Higher classification accuracy and F1 score are always accompanied by  
446 higher  $R^2$  and lower RMSE, showing that CNN-based models perform well in  
447 accurately recognizing true discharge and handling outliers. Among the three models,  
448 CNN is more likely to over- or under-estimate discharge than both CNN+SVM and  
449 CNN+RF, with classification accuracy and F1 score 8.6~13.4% and 0.084~0.115 lower  
450 than CNN+SVM and CNN+RF, respectively. With all environmental conditions taken  
451 into account, CNN+SVM shows the best overall performance with the highest  
452 classification accuracy of 88.6%, the highest F1 score of 0.878, the highest  $R^2$  of 0.989,  
453 and the lowest RMSE of 1.08 dm<sup>3</sup>/s. Such results could be related to the size of our  
454 samples and the characteristics of the features extracted by deep layers of CNN. The  
455 features extracted from stream images under one specific flow discharge show  
456 similarities, which highlights the SVM's capability in classifying the embeddings from  
457 small samples with linear features.

458

### 459 **3.3.3 Comparison of color-enhancing methods**

460 Among the three tested color-enhancing methods, the Color Enhanced approach  
461 generally shows the best performance in discharge classification. Models driven by  
462 Color Enhanced images achieved higher classification accuracy (+2.3%~+7.4%),  
463 higher F1 score (+0.033~+0.067), higher  $R^2$  (+0.001~+0.009), and lower RMSE ( $-$   
464  $0.068 \sim -0.415 \text{ dm}^3/\text{s}$ ) than those driven by images processed with Binarization and  
465 Water-color Enhanced. This is partly due to the different treatments in the edges of the  
466 water body. Binarization and Water-color Enhanced relatively cause larger deviation  
467 from the real edges, while Color Enhanced retains the image information to the  
468 maximum extent. Binarization reduces the cost of discharge computation and data  
469 storage by transforming raw stream images into binary images, and thus facilitates real-  
470 time monitoring by embedded end-to-end devices (e.g., mobile phones) with  
471 insufficient computing power (Shi et al., 2019). Considering that the color and texture  
472 of the water surface vary significantly with discharge volumes while the background is  
473 relatively stable, we proposed the Water-color Enhanced approach that only processes  
474 color information within the water body. In our experiment, it took only 0.0154s to  
475 recognize flow discharge from one Binarization image with an Intel (R) Core (TM) i7-  
476 10750H CPU, which was 36% and 22% faster than that of Color Enhanced and Water-  
477 color Enhanced images, respectively. Such results suggest that it is beneficial to retain  
478 the background information to the maximum extent and include the non-water parts of

479 mountain streams in image processing. However, future applications of image-based  
480 discharge monitoring need to strike a balance between accuracy and speed when  
481 choosing color processing methods.



482

483 **Figure 8.** Performance of discharge classification models under different

484 environmental conditions. Color enhancement methods include Color Enhanced (CE),

485 Binarization (BZ), and Water-color Enhanced (WE).

486

## 487 **4 Discussion**

488 The existing image-based methods usually rely on either the estimations of flow  
489 velocity and cross-section area or assumptions on stage-discharge correlation (Tauro et  
490 al., 2017; Leduc et al., 2018; Davids et al., 2019; Li et al., 2019). The first type of  
491 method uses image-derived surface velocity to estimate sub-sectional mean streamflow  
492 velocity and spatial integration of discharge (Le Coz et al., 2012). The difficulties in  
493 capturing cross-sectional characteristics and the relationship between flow velocity and  
494 water depth limit their application in small mountain streams. The second type of  
495 method retrieves river geometry directly through remote sensing, yet the accuracy is  
496 primarily determined by the empirical assumptions on the relationships among water  
497 depth, velocity, and discharge (Gleason and Smith, 2014; Young et al., 2015). In this  
498 study, we proposed a new camera-based method to directly establish the relationship  
499 between the RGB matrices of stream images and the classification probabilities of  
500 discharge. The unique merit of the CNN-based model is its capability in automatically  
501 extracting and refining discharge-related features from image samples, which improves  
502 the accuracy and applicability of the model. Previous attempts suggest that the selection  
503 of image features can significantly affect the performance on classification of stream  
504 images (Tauro et al., 2014). For example, Chapman et al. (2020) manually extracted  
505 features from pre- and post-weir images and used them as the inputs of machine

506 learning models. However, the dominant image features relating to stream discharge  
507 could vary across different environments (e.g., topography, vegetation on river banks,  
508 water quality), limiting the transferability of such manually identified features.

509 Weather conditions (e.g., sun position, fog, rain) are the most common difficulties  
510 that reduce picture quality (Leduc et al., 2018). Therefore, we designed an automated  
511 procedure for categorizing samples by their brightness and saturation: (a) select four  
512 areas in the image as detection areas, (b) eliminate images with insufficient light or  
513 raindrops on the lens, (c) identify thresholds and classify the remaining images into four  
514 categories for further model training, including the images under the influence of  
515 vegetation shadow and overexposure caused by water reflection in certain angles. Such  
516 inclusion and categorization of defective samples have significantly enhanced the anti-  
517 interference ability of the model, facilitating uninterrupted discharge monitoring  
518 through the daytime. These factors and the thresholds of brightness and saturation are  
519 site-specific and require manual trials to identify them. However, after adequate initial  
520 calibration, an established model can be used for the same site for extended periods and  
521 repeated installations of camera systems.

522 The training and validation of deep learning models require a large number of  
523 representative samples (He et al., 2016). We collected a total of 7757 image samples  
524 from July 20<sup>th</sup> to September 27<sup>th</sup>, 2022, and 3168 images were used for model training  
525 and validation after image screening and categorization. Although we executed an  
526 effective automatic categorization procedure on the acquired image samples, it is

527 undeniable that the training and validation sets didn't cover all environmental  
528 disturbances. For example, the time of sunrise and sunset, the appearance of water  
529 surface reflections, and the coverage of vegetation shadows are affected by the angles  
530 of sunlight and vary with seasons. With sufficient artificial lighting or installation of a  
531 night-vision infrared camera (Royem et al., 2012), the images during nighttime can also  
532 be used for discharge monitoring after training. More image samples are needed to  
533 enrich the representativeness of the model in further studies. Another limitation is that  
534 we have focused on low and average flow conditions in the model training due to the  
535 lack of high-quality flood samples. In tropical and subtropical mountain streams of  
536 southern China, floods usually occur during rainstorms and only last for a short time.  
537 Heavy rainfalls constantly block the camera lens with raindrops, and the rapid  
538 streamflow movement during heavy rainfall tends to cause blurred images, which can  
539 only be partly improved by increasing the shutter speed and adjusting the camera  
540 position. Moreover, site-specific field data is crucial for identifying the criteria for  
541 image categorization and model training, which restricts the broader applicability of  
542 our approach in ungauged basins, where such field data may not be readily available.  
543 Further research on integrating multiple data sources and surveying approaches is  
544 warranted for developing a more generalizable method.

## 545 **5 Conclusions**

546 This study presents a novel method for discharge monitoring of mountain streams using  
547 deep learning techniques and a low-cost solar-powered commercial camera

548 (approximately \$200). The results confirmed our hypothesis that the discharge-relevant  
549 stream features embedded in a large number of RGB images can be implicitly  
550 recognized and retrieved by CNN to achieve continuous discharge monitoring.  
551 Coupling CNN and traditional machine learning methods can potentially improve  
552 model performance in discharge classification to various extents. In this case, the  
553 classification accuracy, F1 score, and  $R^2$  of CNN+SVM and CNN+RF were  
554 9.1%~14.4%, 0.084~0.115, and 0.006~0.010 higher, respectively, while RMSE was  
555 0.31~0.51  $\text{dm}^3/\text{s}$  lower compared to CNN. Proper image pre-processing and  
556 categorization can largely enhance the applicability of image-based discharge  
557 monitoring. In an environment under complex disturbances such as mountain streams,  
558 image quality is constantly interfered with by shadows of vegetation on the river banks.  
559 The automated image categorization procedure can effectively recognize discharge  
560 from defective images by filtering samples under different conditions and improve  
561 model robustness. The comparison of the three color-enhancing approaches also  
562 confirms the importance of including the non-water parts (e.g., large rocks) and  
563 retaining the background information to the maximum extent in the image analysis.

564 The proposed method provides an inexpensive and flexible alternative apparatus for  
565 continuous discharge monitoring at rocky upstream mountain streams, where it is  
566 challenging to identify the cross-section shape or establish a stable stage-discharge  
567 relationship. Site-specific field data is needed to identify the criteria for image  
568 categorization and model validation. However, it circumvents the potential errors in



569 assuming cross-section characteristics, such as the relationship between water depth  
570 and flow velocity, and represents a new direction for applying deep learning techniques  
571 in acquiring high-frequency discharge data through image analysis.

572

### 573 **Code/Data availability**

574 The code and data are available upon request from the corresponding author.

### 575 **Author contribution**

576 KD and CF conceptualized the experiments. GY, ZZ, and QZ curated the data. All  
577 authors participated in the investigation. CF, GY, ZZ, and QZ wrote the original draft  
578 and visualized the data. KD reviewed and edited the final version of the manuscript.

### 579 **Competing interests**

580 The authors declare no competing interests.

### 581 **Acknowledgments**

582 This work was supported by the National Key Research and Development Program of  
583 China (2021YFC3200205, 2021YFC3001000), the National Natural Science  
584 Foundation of China (52379032), the Guangdong Basic and Applied Basic Research  
585 Foundation (2023A1515012241, 2023B1515040028), and the Guangdong Provincial  
586 Department of Science and Technology (2019ZT08G090).

587

## 588 **References**

- 589 Abdullah-Al-Wadud, M., Kabir, M. H., Dewan, M. A. A., and Chae, O.: A Dynamic  
590 Histogram Equalization for Image Contrast Enhancement, *IEEE Transactions on*  
591 *Consumer Electronics*, 53, 593-600, 10.1109/TCE.2007.381734, 2007.
- 592 Ansari, S., Rennie, C., Jamieson, E., Seidou, O., and Clark, S.: RivQNet: Deep Learning  
593 Based River Discharge Estimation Using Close - Range Water Surface Imagery,  
594 *Water Resources Research*, 59, 10.1029/2021WR031841, 2023.
- 595 Aslam, J. A., Popa, R. A., and Rivest, R. L.: On estimating the size and confidence of a  
596 statistical audit, *Proceedings of the USENIX Workshop on Accurate Electronic*  
597 *Voting Technology*, Boston, MA, 10.5555/1323111.1323119, 2007.
- 598 Breiman, L.: Random Forests, *Machine Learning*, 45, 5-32, 10.1023/A:1010933404324,  
599 2001.
- 600 Burges, C. J. C.: A Tutorial on Support Vector Machines for Pattern Recognition, *Data*  
601 *Mining and Knowledge Discovery*, 2, 121-167, 10.1023/A:1009715923555, 1998.
- 602 Canziani, A., Paszke, A., and Culurciello, E.: An Analysis of Deep Neural Network  
603 Models for Practical Applications, *ArXiv*, abs/1605.07678, 7-14,  
604 10.48550/arXiv.1605.07678, 2016.
- 605 Carlisle, D., Grantham, T. E., Eng, K., and Wolock, D. M.: Biological relevance of  
606 streamflow metrics: Regional and national perspectives, *Freshwater Science*, 36,  
607 927-940, 10.1086/694913, 2017.
- 608 Chang, F., Hong, W., Zhang, T., Jing, J., and Liu, X.: Research on Wavelet Denoising  
609 for Pulse Signal Based on Improved Wavelet Thresholding, 2010 First International  
610 Conference on Pervasive Computing, Signal Processing and Applications, Harbin,  
611 China, 17-19 Sept. 2010, 564-567, 10.1109/PCSPA.2010.142, 2010.
- 612 Chapman, K. W., Gilmore, T. E., Chapman, C. D., Mehrubeoglu, M., and Mittelstet, A.  
613 R.: Camera-based Water Stage and Discharge Prediction with Machine Learning,  
614 *Hydrol. Earth Syst. Sci. Discuss.*, 2020, 1-28, 10.5194/hess-2020-575, 2020.

615 Cheng, H. D. and Shi, X. J.: A simple and effective histogram equalization approach to  
616 image enhancement, *Digital Signal Processing*, 14, 158-170,  
617 10.1016/j.dsp.2003.07.002, 2004.

618 Clarke, R. T.: Uncertainty in the estimation of mean annual flood due to rating-curve  
619 indefiniton, *Journal of Hydrology*, 222, 185-190, 10.1016/S0022-1694(99)00097-9,  
620 1999.

621 Cortes, C. and Vapnik, V.: Support-vector networks, *Machine Learning*, 20, 273-297,  
622 10.1007/bf00994018, 1995.

623 Council, N. R.: Assessing the national streamflow information program, National  
624 Academies Press, 176 pp., 10.17226/10967, 2004.

625 Czuba, J. A., Fofoula-Georgiou, E., Gran, K. B., Belmont, P., and Wilcock, P. R.:  
626 Interplay between spatially explicit sediment sourcing, hierarchical river-network  
627 structure, and in-channel bed material sediment transport and storage dynamics,  
628 *Journal of Geophysical Research: Earth Surface*, 122, 1090-1120,  
629 10.1002/2016jf003965, 2017.

630 Davids, J. C., Rutten, M. M., Pandey, A., Devkota, N., van Oyen, W. D., Prajapati, R.,  
631 and van de Giesen, N.: Citizen science flow – an assessment of simple streamflow  
632 measurement methods, *Hydrology and Earth System Sciences*, 23, 1045-1065,  
633 10.5194/hess-23-1045-2019, 2019.

634 Deweber, J. T., Tsang, Y. P., Krueger, D. M., Whittier, J. B., Wagner, T., Infante, D. M.,  
635 and Whelan, G.: Importance of Understanding Landscape Biases in USGS Gage  
636 Locations: Implications and Solutions for Managers, *Fisheries*, 39, 155-163,  
637 10.1080/03632415.2014.891503, 2014.

638 Finlayson, G. D., Hordley, S. D., and Drew, M. S.: Removing Shadows from Images,  
639 *Computer Vision — ECCV 2002*, Berlin, Heidelberg, 2002, 823-836, 10.1007/3-  
640 540-47979-1\_55, 2002.

641 Fujita, I., Muste, M., and Kruger, A.: Large-scale particle image velocimetry for flow  
642 analysis in hydraulic engineering applications, *Journal of Hydraulic Research*, 36,

643 397-414, 10.1080/00221689809498626, 2010.

644 Fujita, I., Watanabe, H., and Tsubaki, R.: Development of a non-intrusive and efficient  
645 flow monitoring technique: The space-time image velocimetry (STIV), *International*  
646 *Journal of River Basin Management*, 5, 105-114, 10.1080/15715124.2007.9635310,  
647 2007.

648 Gershon, R., Jepson, A. D., and Tsotsos, J. K.: Ambient illumination and the  
649 determination of material changes, *J Opt Soc Am A*, 3, 1700-1707,  
650 10.1364/josaa.3.001700, 1986.

651 Gleason, C. J. and Smith, L. C.: Toward global mapping of river discharge using  
652 satellite images and at-many-stations hydraulic geometry, *Proceedings of the*  
653 *National Academy of Sciences*, 111, 4788-4791, 10.1073/pnas.1317606111, 2014.

654 Hanczar, B., Hua, J., Sima, C., Weinstein, J., Bittner, M., and Dougherty, E. R.: Small-  
655 sample precision of ROC-related estimates, *Bioinformatics*, 26, 822-830,  
656 10.1093/bioinformatics/btq037, 2010.

657 Hannah, D. M., Demuth, S., van Lanen, H. A. J., Looser, U., Prudhomme, C., Rees, G.,  
658 Stahl, K., and Tallaksen, L. M.: Large-scale river flow archives: importance, current  
659 status and future needs, *Hydrological Processes*, 25, 1191-1200, 10.1002/hyp.7794,  
660 2011.

661 He, K., Zhang, X., Ren, S., and Sun, J.: Deep residual learning for image recognition,  
662 *Proceedings of the IEEE conference on computer vision and pattern recognition*, Las  
663 Vegas, NV, USA, 770-778, 10.1109/cvpr.2016.90, 2016.

664 Heaton, J.: Ian Goodfellow, Yoshua Bengio, and Aaron Courville: *Deep learning: The*  
665 *MIT Press, Genetic programming and evolvable machines*, 19, 305-307,  
666 10.1007/s10710-017-9314-z, 2018.

667 Herzog, A., Stahl, K., Blauhut, V., and Weiler, M.: Measuring zero water level in stream  
668 reaches: A comparison of an image-based versus a conventional method,  
669 *Hydrological Processes*, 36, e14234, 10.1002/hyp.14658, 2022.

670 Jiang, P. T., Zhang, C. B., Hou, Q., Cheng, M. M., and Wei, Y.: LayerCAM: Exploring

671 Hierarchical Class Activation Maps for Localization, *IEEE Transactions on Image*  
672 *Processing*, 30, 5875-5888, 10.1109/TIP.2021.3089943, 2021.

673 Karvonen, J.: Virtual radar ice buoys – a method for measuring fine-scale sea ice drift,  
674 *The Cryosphere*, 10, 29-42, 10.5194/tc-10-29-2016, 2016.

675 Kasuga, K., Hachiya, H., and Kinoshita, T.: Quantitative Estimation of the Ultrasound  
676 Transmission Characteristics for River Flow Measurement during a Flood, *Japanese*  
677 *Journal of Applied Physics*, 42, 3212-3215, 10.1143/jjap.42.3212, 2003.

678 Keskar, N., Mudigere, D., Nocedal, J., Smelyanskiy, M., and Tang, P.: On Large-Batch  
679 Training for Deep Learning: Generalization Gap and Sharp Minima, arXiv preprint  
680 arXiv:1609.04836, 10.48550/arXiv.1609.04836, 2016.

681 Kim, W., Roh, S.-H., Moon, Y., and Jung, S.: Evaluation of Rededge-M Camera for  
682 Water Color Observation after Image Preprocessing, *Journal of the Korean Society*  
683 *of Surveying Geodesy Photogrammetry and Cartography*, 37, 167-175,  
684 10.7848/ksgpc.2019.37.3.167, 2019.

685 Krizhevsky, A., Sutskever, I., and Hinton, G. E.: ImageNet classification with deep  
686 convolutional neural networks, *Communications of the ACM*, 60, 84-90,  
687 10.1145/3065386, 2017.

688 Le Coz, J., Camenen, B., Peyrard, X., and Dramais, G.: Uncertainty in open-channel  
689 discharges measured with the velocity–area method, *Flow Measurement and*  
690 *Instrumentation*, 26, 18-29, 10.1016/j.flowmeasinst.2012.05.001, 2012.

691 LeCun, Y., Bengio, Y., and Hinton, G.: Deep learning, *Nature*, 521, 436-444,  
692 10.1038/nature14539, 2015.

693 Leduc, P., Ashmore, P., and Sjogren, D.: Technical note: Stage and water width  
694 measurement of a mountain stream using a simple time-lapse camera, *Hydrology and*  
695 *Earth System Sciences*, 22, 1-11, 10.5194/hess-22-1-2018, 2018.

696 Li, W., Liao, Q., and Ran, Q.: Stereo-imaging LSPIV (SI-LSPIV) for 3D water surface  
697 reconstruction and discharge measurement in mountain river flows, *Journal of*  
698 *Hydrology*, 578, 124099, 10.1016/j.jhydrol.2019.124099, 2019.

699 Matykiewicz, P. and Pestian, J.: Effect of small sample size on text categorization with  
700 support vector machines, *Publication History*, 193-201 pp.,  
701 10.5555/2391123.2391149, 2012.

702 McMillan, H., Freer, J., Pappenberger, F., Krueger, T., and Clark, M.: Impacts of  
703 uncertain river flow data on rainfall-runoff model calibration and discharge  
704 predictions, *Hydrological Processes: An International Journal*, 24, 1270-1284,  
705 10.1002/hyp.7587, 2010.

706 Noto, S., Tauro, F., Petroselli, A., Apollonio, C., Botter, G., and Grimaldi, S.: Low-cost  
707 stage-camera system for continuous water-level monitoring in ephemeral streams,  
708 *Hydrological Sciences Journal*, 67, 1439-1448, 10.1080/02626667.2022.2079415,  
709 2022.

710 Panda, B., Herbach, J., Basu, S., and Bayardo, R.: PLANET: Massively parallel  
711 learning of tree ensembles with MapReduce, *PVLDB*, 2, 1426-1437,  
712 10.14778/1687553.1687569, 2009.

713 Royem, A. A., Mui, C. K., Fuka, D. R., and Walter, M. T.: Technical Note: Proposing a  
714 Low-Tech, Affordable, Accurate Stream Stage Monitoring System, *Transactions of*  
715 *the ASABE*, 55, 2237-2242, 10.13031/2013.42512, 2012.

716 Sauvola, J. and Pietikäinen, M.: Adaptive document image binarization, *Pattern*  
717 *Recognition*, 33, 225-236, 10.1016/s0031-3203(99)00055-2, 2000.

718 Shi, W., Jiang, F., Liu, S., and Zhao, D.: Image Compressed Sensing using  
719 Convolutional Neural Network, *IEEE Trans Image Process*, 29, 375-388,  
720 10.1109/TIP.2019.2928136, 2019.

721 Tauro, F., Grimaldi, S., and Porfiri, M.: Unraveling flow patterns through nonlinear  
722 manifold learning, *PLoS One*, 9, e91131, 10.1371/journal.pone.0091131, 2014.

723 Tauro, F., Piscopia, R., and Grimaldi, S.: Streamflow Observations From Cameras:  
724 Large-Scale Particle Image Velocimetry or Particle Tracking Velocimetry?, *Water*  
725 *Resources Research*, 53, 10374-10394, 10.1002/2017wr020848, 2017.

726 Tauro, F., Tosi, F., Mattoccia, S., Toth, E., Piscopia, R., and Grimaldi, S.: Optical

727 Tracking Velocimetry (OTV): Leveraging Optical Flow and Trajectory-Based  
728 Filtering for Surface Streamflow Observations, *Remote Sensing*, 10, 2010,  
729 10.3390/rs10122010, 2018.

730 Tin Kam, H.: Random decision forests, *Proceedings of 3rd International Conference on*  
731 *Document Analysis and Recognition*, Montreal, QC, Canada, 14-16 Aug. 1995, 278-  
732 282 vol.271, 10.1109/ICDAR.1995.598994, 1995.

733 Tsubaki, R.: On the Texture Angle Detection Used in Space-Time Image Velocimetry  
734 (STIV), *Water Resources Research*, 53, 10908-10914, 10.1002/2017wr021913, 2017.

735 Wang, R., Chaudhari, P., and Davatzikos, C.: Bias in machine learning models can be  
736 significantly mitigated by careful training: Evidence from neuroimaging studies,  
737 *Proceedings of the National Academy of Sciences*, 120, e2211613120,  
738 10.1073/pnas.2211613120, 2023.

739 Yorke, T. H. and Oberg, K. A.: Measuring river velocity and discharge with acoustic  
740 Doppler profilers, *Flow Measurement and Instrumentation*, 13, 191-195,  
741 10.1016/s0955-5986(02)00051-1, 2002.

742 Young, D. S., Hart, J. K., and Martinez, K.: Image analysis techniques to estimate river  
743 discharge using time-lapse cameras in remote locations, *Computers & Geosciences*,  
744 76, 1-10, 10.1016/j.cageo.2014.11.008, 2015.

745 Zhang, D.: *Fundamentals of Image Data Mining, Analysis, Features, Classification and*  
746 *Retrieval*, Springer, 7, 35-44, 10.1007/978-3-030-17989-2, 2019.

747